MAX-PLANCK-INSTITUT FÜR PLASMAPHYSIK

GARCHING BEI MÜNCHEN

Two-Fluid Simulation of Expansion and
Confinement of Pellet-Produced Hydrogen
Clouds in Hot Magnetized Plasmas

G. Kristof

IPP 5/73   Dezember 1996

Home address: Technical University of Budapest, Hungary

ABSTRACT

The structure of dense particle clouds surrounding ablating hydrogen isotope pellets is investigated with primary attention to the B-perpendicular expansion and deceleration dynamics. In order to distinguish between the cross-field (radial) motion of charged particles and that of neutrals, the model is based on a two-fluid approximation. A 1.5-D Lagrangian numerical method is used for solving the system of MHD equations. The characteristic cloud radius and radial distributions of temperature, particle densities, and other flow properties are calculated by means of this two-fluid - single-temperature model. The results show that collisional coupling between the neutral and ionized components is strong enough to change the initially spherically symmetric expansion of the neutral particles to a field-aligned flow pattern, in agreement with the experimentally observed elongated radiation emission patterns of the excited neutral atoms. Calculated clouds parameters are compared with measured data and with results stemming from comparative calculations.

1. INTRODUCTION

Hydrogen pellets moving in hot magnetized plasmas usually produce cigar-shaped visible clouds of consisting of excited neutral particles.
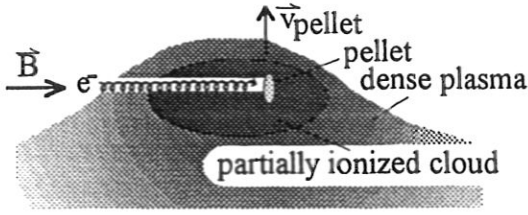

Fig.1.

Outside the visible cloud, a dense plasma fan exists that is kept back by the magnetic field relative to the moving pellet. (Drift phenomena are not considered in this analysis.) Hot plasma electrons can penetrate deeply into the cloud, reaching in some cases the surface of the pellet. The stopping length of the hot electrons may be calculated by means of loss functions [1], as has been done in the present work, or on the basis of kinetic theory. As shown previously [2], the line-density of the shielding cloud calculated along the particular field line that crosses the centre of the pellet plays an important role in the ablation process. Accurate determination of the ablation rate should require, in general, information on the three-dimensional density and temperature distributions in the shielding cloud surrounding the pellet. However, due to the variations of temperature and density over several orders of magnitude within the cloud, numerical difficulties and substantial computer times must be taken into account when solving the corresponding 3-D MHD conservation equations. It is therefore of practical interest to seek simpler but still reliable 1, 1.5, and 2-D approximations.

Good estimates can be obtained for the ablation rate on the basis of calculations pertaining to the energy transport to the pellet within the flux tube confining the partially or fully ionized ablation cloud. The first step to such calculations is the determination of the flux tube radius, which is approximately equal to the ionization and/or confinement radius in the B-perp direction, and of the resulting residence time of the pellet in this flux tube, which is given by the flux tube diameter and the pellet velocity [2], [3].

The ionization radius can be obtained from MHD calculations by neglecting the velocity of the pellet against he the expansion velocity of the expanding ablatant (10^3 vs 10^4 m/s) and thus assuming axially symmetric flow in the ablation cloud. A number of time dependent simulation codes have been developed since 1988, most of them based on Lagrangian approach (see e.g. [3 to 8], and [9]). The numerical schemes used and thus the physical processes taken into acount in the various simulation codes are different. Depending on the numerics and physics used, different domains of tokamak plasma parameters (density, temperature, and magnetic field strength) can be covered. In a typical time-dependent Lagrangian simulation, it is usually assumed that the pellet is initially surrounded by a small neutral cloud incorporating not more than 5 per-cent (at most) of the pellet mass to be ablated. The pellet is represented by a neutral particle source of finite size that feeds particles to the cloud cells that are in contact with the source. As the temperature increases, the cloud undegoes an approximately spherical expansion until ionization sets-in beginning usually at the cloud's periphery. The cross-field motion of the ionized fluid induces a current in the poloidal direction (around the axis of symmetry, which is aligned with the magnetic field lines).
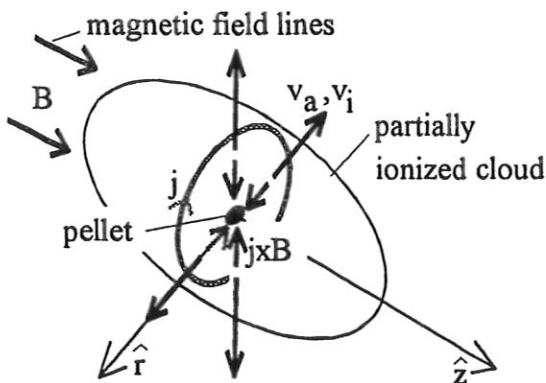
Fig.2.

The $\vec{j} \times \vec{B}$ force acting on the ionized fraction of the pellet cloud decelerates the cross-flow. After the radial motion is stopped, the expansion process continues along the magnetic field lines. Due to the kinetic energy stored in the radially expanding partially ionized cloud and the relatively slow diffusion (rediffusion) of the magnetic field into the cloud, the magnetic field strength may be reduced in the cloud interior and a partial magnetic cavity may form there.

The aim of the present work is the determination, as accurate as possible, of the transverse (B-perp) deceleration dynamics of pellet clouds in magnetized hot plasmas and of the resulting time-dependent cloud parameter distributions by cosidering the neutral and ionized cloud components separately. The two cloud constituents are coupled by collisional interaction.

Due to the high collisionality, the two fluids are assumed to have a single temperature. In the following sections, the mathematical model used in the computations shall be described and the results of calculations shall be compared with those obtained by other models and with some experimental data. The considerations are limited to hydrogen isotope (deuterium) plasmas.

2. MATHEMATICAL MODEL

2.1 Lagrangian system based on two-fluid approximation

Detailed descriptions of one-dimensional Lagrangian simulations of the radial expansion dynamics can be found in the literature (see, for example, [3], [6]). We shall focus here on the two-fluid features of the model used in the present calculations.

Ions and electrons may have fluid velocities in the radial direction different from those of the neutral particles. Charged and neutral particles are assumed to be two distinct fluid components that are coupled through collisional momentum transfer. In the case of a low density cloud (low collisionality) , the radial velocity of the neutral component (v_a) can be significantly higher than the radial velocity of the charged component (v_i). Both fluid components are assumed to have the same temperature and the same velocity (v_z) in the axial direction. The vectors $\vec{v}_i$ and $\vec{v}_a$ are velocity vectors of the corresponding components: $\vec{v}_i = v_i \hat{r} + v_z \hat{z}$ and $\vec{v}_a = v_a \hat{r} + v_z \hat{z}$.

In general, Lagrangian approximation to a two-component fluid would require two mesh systems, i.e. two arrays of Lagrangian cells, interacting with each other. In this case, special algorithms would be required to determine the boundaries of volume fractions interacting with each other and the lumped cell properties resulting from this interaction. To avoid the tedious numerics associated with such an approach a novel method was introduced and used in the present work: a single mesh system defined in such a way that the flux of heavy particles across the cell boundaries becomes identical to zero. This way a characteristic property of Lagrangian systems -constant cell mass - is preserved (except in the source region).

In the model discussed here, each cell boundary is moved with a particular velocity at which the neutral flux crossing the cell boundary from one side is balanced by the ion flux coming from the other side:

$$n_a(\vec{v}_a - \vec{v}) + n_i(\vec{v}_i - \vec{v}) = 0.$$

3

which yields for the propagational velocity of the cell boundary

$$\vec{v} = \alpha\,\vec{v}_i + (1-\alpha)\vec{v}_a$$

where alpha denotes the degree of ionization:

$$\alpha = \frac{n_i}{n_i + n_a}.$$

We denote the radial component of $\vec{v}$ by v_r, so that the radial velocity of the grid can be evaluated as a weighted function of the ionization degree (no coordinate subscripts are used for the radial velocities):
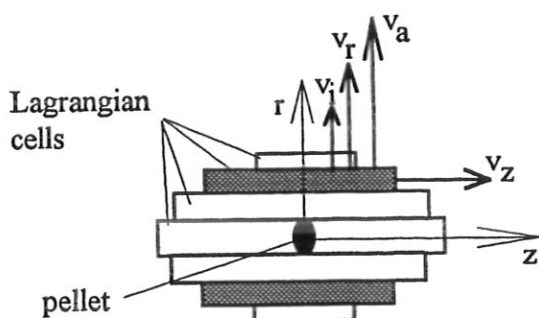
$$v_r = \alpha\,v_i + (1-\alpha)v_a$$

Fig.3.

The numerical cells are in a coaxial arrangement. They are allowed to change their radial position and length. The axial distributions of the flow properties are not calculated (single cell approximation in the axial direction). The velocity of the axial expansion (v_z) is calculated in terms of the z-averaged density and pressure values for every annular cell (1.5-D model). The number of cells was continuously increased during the simulation. Artificial viscosity was used, if needed, in the numerical scheme.

2.2 Governing equations

In order to describe the motion of a partially ionized and relatively high-density fluid in a magnetic field, the usual conservation equations (mass, momentum, energy) are supplemented by Ohm's law, Maxwell's equations (used for determining the time variation of the magnetic field distribution), and finite-rate ionization and recombination rate equations. Two continuity equations were used for calculating the heavy particle density $n_H = n_a + n_i$ and the ion (electron) density separately:

$$\frac{\partial(\rho_i + \rho_a)}{\partial t} + \nabla\cdot(\rho_i\,\vec{v}_i + \rho_a\,\vec{v}_a) = \dot{m}_s, \quad \frac{\partial \rho_i}{\partial t} + \nabla\cdot(\rho_i\,\vec{v}_i) = m(\dot{I} - \dot{R}).$$

where m denotes particle mass, $m_i \cong m_a$, $\rho = m\cdot n$, and, in the case of hydrogen isotope plasmas, $n_e = n_i$. Indices i, a, and e denote ions, neutrals (atoms), and electrons, respectively.
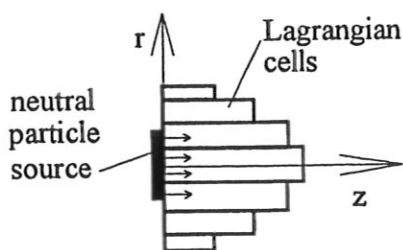

Fig.4.

The quantity $\dot{m}_s$ is the mass deposition rate per unit volume produced by the neutral particle source representing the pellet. In the present code, the mass deposition rate $\dot{m}_s$ is assumed to be given, hence the dependence of the ablation rate on the plasma parameters is not modelled. The size of the mass source, equal to the pellet radius, is specified. The particles released by the mass source are fed into the Lagrangian cells which are still in contact with the source ($r < r_{pellet}$). The number of particles fed to a Lagrangian cell is proportional to the area of the source-cell contact surface.

The momentum equations of the neutral and charged particles are as follows:

$$\frac{\partial}{\partial t}(\rho_a \vec{v}_a) + \nabla \cdot \left(\rho_a \vec{v}_a \otimes \vec{v}_a + p_a \overline{\overline{I}} - \overline{\overline{\tau}}_a\right) = \dot{m}_s \vec{v}_s - \vec{f}_{ai}$$

$$\frac{\partial}{\partial t}(\rho_i \vec{v}_i) + \nabla \cdot \left(\rho_i \vec{v}_i \otimes \vec{v}_i + p_i \overline{\overline{I}} - \overline{\overline{\tau}}_i\right) = \vec{j} \times \vec{B} + \vec{f}_{ai}$$

The term $\vec{f}_{ai}$ coupling the components describes the momentum transfer caused by collisions as well as ionization and recombination events.

The energy equations of all constituents (electrons, ions, and neutrals) are summed-up and solved for the common temperature (single temperature model):

$$\frac{\partial}{\partial t}\left([n_a + 2n_i]\frac{kT}{\gamma - 1}\right) + \nabla \cdot \left([n_a\vec{v}_a + 2n_i\vec{v}_i]\frac{kT}{\gamma - 1}\right) = -n_a kT \nabla \cdot \vec{v}_a - 2n_i kT \nabla \cdot \vec{v}_i + \dot{Q}.$$

In the above expression, $\dot{Q}$ denotes the sum of the heat deposition rate, the power spent on ionization, viscous dissipation, ohmic heating, and the rate of energy supplied by the source particles. The local rate of heat deposition is calculated by taking into account conductive heat transport in the radial direction and corpuscular heat transport by plasma electrons in the axial (B-parallel) direction. The energy flux carried by the electrons is flux-limited (by a factor of 0.5) and is also limited by possible shine-through effect.

The finite-rate ionization and recombination processes cosidered include electron impact ionization and three-body recombination as well as photo-ionization and radiative recombination. The respective rate coefficients were taken from previous pellet calculations (see [3] to [5]).

An equation is obtained from Maxwell's equations and Ohm's law for the diffusion rate of the magnetic field:

$$\frac{\partial \vec{B}}{\partial t} = -\nabla \times \left(\chi_m \nabla \times \vec{B}\right) + \nabla \times \left(\vec{v}_i \times \vec{B}\right).$$

where $\chi_m = \dfrac{1}{\mu_0 \sigma}$ is the diffusion coefficient of the magnetic field. In the present work, the Spitzer conductivity value was used. The one-dimensional (radial) magnetic field distribution is calculated in an approximation corresponding to an infinitely long cylindrical plasmoid.

2.3 Approximations to the Lorenz force

There are various approximations available for calculating the Lorenz force $\vec{j} \times \vec{B}$ appearing in the ion momentum equation.

In the simplest approximation corresponding to zero interaction between the magnetic field and the cloud plasma (vanishingly small beta values), one may neglect the perturbation of the magnetic field distribution and use Ohm's law with the electric field set to zero (short-circuit condition in the poloidal direction):

$$\left(\vec{j} \times \vec{B}\right) \cdot \hat{r} = -\sigma v_i B_0^2 \tag{a}$$

In the next approximation, the magnetic field distribution is calculated by means of the diffusion equation, but the inductive electric field associated with the time variation of the magnetic field is still neglected:

$$\left(\vec{j} \times \vec{B}\right) \cdot \hat{r} = -\sigma v_i B^2 \tag{b}$$

For the case when the variation of the magnetic field (temporal and spatial) cannot be neglected, the equation for the Lorenz force follows from Maxwell's equations and can be given in terms of the gradient of the magnetic pressure:

with p_m defined as $p_m = \dfrac{B^2}{2\mu_0}$ we have

$$\left(\vec{j} \times \vec{B}\right) \cdot \hat{r} = -\frac{\partial p_m}{\partial r} \tag{c}$$

For the sake of comparison, in a number of scenarios all three aproximations were used. The results are discussed in the following sections.

2.4 Collisional interaction between the components

The interaction between the neutral and ionized components is represented by the term $\vec{f}_{ai}$ which includes two effects: a source-like term associated with the transfer of momentum from one component to the other at each ionization and/or recombination event, and a term associated with collisional momentum transfer:

$$\vec{f}_{ai} = \vec{f}_{ai,IR} + \vec{f}_{ai,coll}.$$

Every ionization and/or recombination event transfers momentum from one component to the other. Considering the momentum gained by the ionized component due to ionization or recombination events (equal to the momentum lost by the neutral component) we have:

$$\vec{f}_{ai,IR} = \dot{I} m \vec{v}_a - \dot{R} m \vec{v}_i$$

The collisional momentum transfer $\vec{f}_{ai,coll}$ is calculated by taking into account electron-neutral and ion-neutral collisions:

$$\vec{f}_{ai,coll} = \vec{P}_{ae} + \vec{P}_{ai} = \frac{4}{3} n_e n_a \left|v_{ea}\right| \sigma_{ea} m_{ea} \left(\vec{v}_a - \vec{v}_i\right) +$$

$$+ \frac{4}{3} n_i n_a \left|v_{ia}\right| \sigma_{ia} m_{ia} \left(\vec{v}_a - \vec{v}_i\right)$$

Defining the reduced masses and the effective temperatures as

$$m_{ea} = \frac{m_e m_a}{m_e + m_a} \cong m_e, \text{ for } m_{ia} = \frac{m_i m_a}{m_i + m_a} \cong \frac{m}{2},$$

$$T_{ea} = m_{ea}\left(\frac{T_e}{m_e} + \frac{T_a}{m_a}\right) \cong T, \text{ for } T_{ia} = m_{ia}\left(\frac{T_i}{m_i} + \frac{T_a}{m_a}\right) \cong T.$$

The relative flow velocities v_{ea} and v_{ia} can be approximated with the help of the respective thermal velocities:

$$\left|v_{ia}\right| = \left(\frac{8kT}{\pi m_{ia}} + \left(v_i - v_a\right)^2\right)^{\frac{1}{2}} \cong \sqrt{\frac{16kT}{\pi m}}, \qquad \left|v_{ea}\right| \cong \sqrt{\frac{8kT}{\pi m_e}}.$$

The collisional cross-section used for electron-neutral and ion-neutral elastic collisions are as follows (see, for example, [10]):

$$\sigma_{ea} = \begin{cases} \dfrac{3 \cdot 10^{-17}}{\sqrt{T[K]}} \left[m^2\right], & \text{ha } T > 4.64 \cdot 10^4 \left[K\right] \\[3mm] \dfrac{3 \cdot 10^{-17}}{\sqrt{4.64 \cdot 10^4}} \left[m^2\right], & \text{ha } T \le 4.64 \cdot 10^4 \left[K\right] \end{cases},$$

$$\sigma_{ia} = 4.486 \cdot 10^{-20} \left(1 + \dfrac{7.227 \cdot 10^8}{\dfrac{16 \, kT}{\pi \, m}} \right).$$

2.5 Approximations to collisional interaction

For checking the strength of collisional coupling, comparative calculations were made in some scenarios based on three different approaches:

(a) Strong collisional coupling. In this case $v_a = v_i$ was assumed and the two momentum equations were added. The system was thus reduced to a single-fluid model.

(b) Instantaneous ion deceleration. In this case it was assumed that the ions are stopped instantaneously by the magnetic field at the locus of their birth and $v_i = 0$ was assumed in the subsequent calculations. The ions serve in this case only as collision centers.

(c) The full two-fluid model considered in the present work. The results of comparative calculations are described in the next sections.

3. RESULTS AND DISCUSSION

In this section, first we describe results of scenario calculations obtained with the present model and then perform comparison with other models and with measured data.

3.1 Time evolution of the cloud

In Fig.5., the radial distributions of the particle densities, radial velocities, radial momenta, cloud temperature, and of the Mach number based on the radial velocity are given for three different times (time evolution): $t = 0.3$ μs, 0.66 μs, and 0.9 μs. The plasma parameters, field strength, and particle source strength (ablation rate) used in these simulations are as follows:

$$n_{e0} = 5 \cdot 10^{19} \, m^{-3}, \quad T_{e0} = 500 \, eV; \quad B_0 = 2 \, T; \quad \dot{n}_s = 2 \cdot 10^{23} \, s^{-1}; \quad r_{pellet} = 1 \, mm .$$

The line types used for the different time levels are:

——————— $t = 0.3\,\mu s$, ·············· $t = 0.6\,\mu s$, ——————— $t = 0.9\,\mu s$
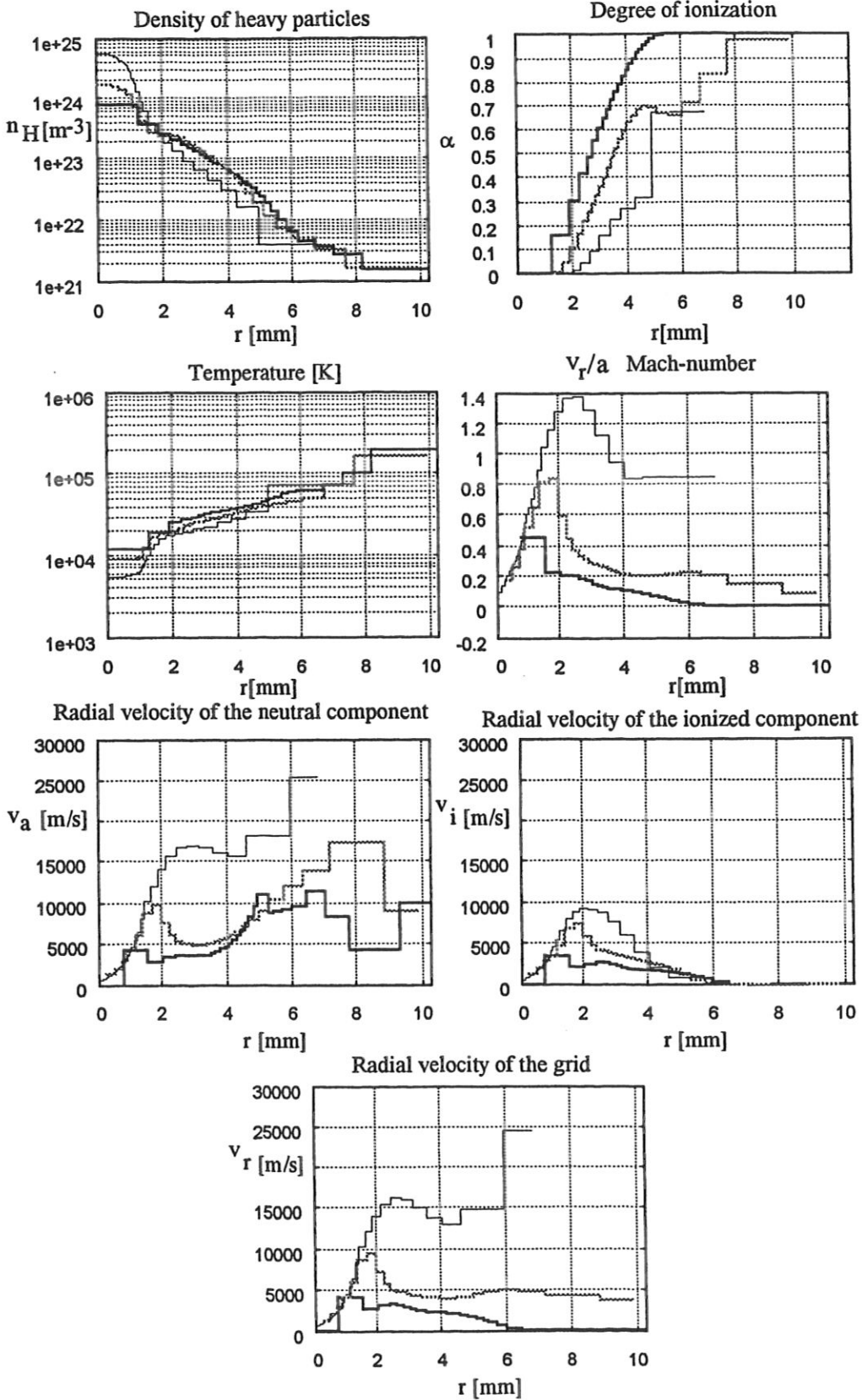

Fig.5.

The heavy particle density resembles an exponential function of the radius, changing at least three orders of magnitude. The temperature is a monotonously increasing function of the

radius whereas the Mach number has a maximum at a certain radial position, this position shifts with time towards the centre. At the beginning of the ionization process, the neutral fluid component may move significantly faster than the ionized fluid component.
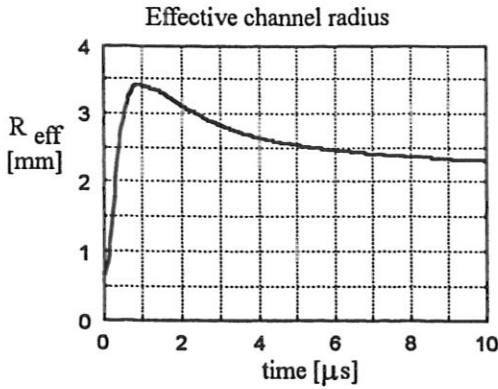
Effective channel radius

Fig.6.

Since the radial expansion of the ionized matter is first stopped at the periphery, and this deceleration 'wave' propagates subsequently from the periphery into the cloud interior, the effective channel cross-section of the axial (B−parallel) flow may change in time. Fig.6. shows the time variation of the effective cross-section for momentum transfer in the axial direction defined as

$$R_{chn} = \frac{\int r \cdot v_z(\rho_a + \rho_i) dV}{\int v_z(\rho_a + \rho_i) dV}.$$

As can be seen, a notable change of the effective cross-section may take place. (The parameters used in this simulation are the same as in the case of Fig.5 except the simulation time is 10 μs.)

Due to the initially fast radial flow of the neutral component, the cloud has a low-density peripheral layer. (Note that the flow is in general subsonic, in spite of the high v_r values.)
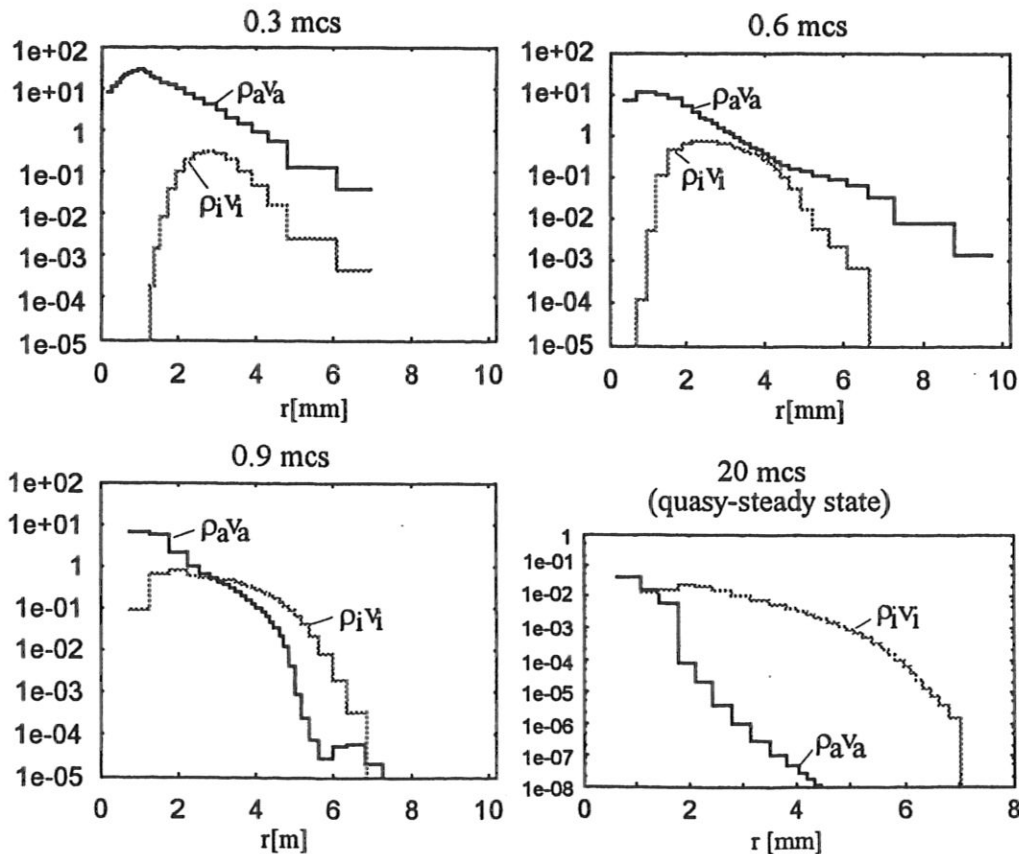

Fig.7.

In Fig.7, the specific momenta of the two components (in $kg \cdot m^{-2} \cdot s^{-1}$ units) are plotted for time levels 0.3 μs, 0.6 μs, 0.9 μs and 20 μs. The neutral fluid originating from the surface of the pellet cannot penetrate through the highly ionized outer region. Comparing the specific momenta curves of different time levels, one sees that a quasi-steady flow develops after 5 to 10 mcrs characterized by the balance between the particle source and the field-aligned out-flow

9

of the particles supplied to the cloud. In this respect, no significant differences were fond between the results of single-fluid and two-fluid approximations.

3.2 The characteristic cloud radius

We define the characteristic size of the cloud ($R_{99\%}$) as the radius of a field-aligned cylinder containing 99% of the total mass. The values of $R_{99\%}$ in millimetres (radial deceleration is completed) as a function of $\dot{n}_s, T_{e0}, B_0$ is plotted in Fig.8.
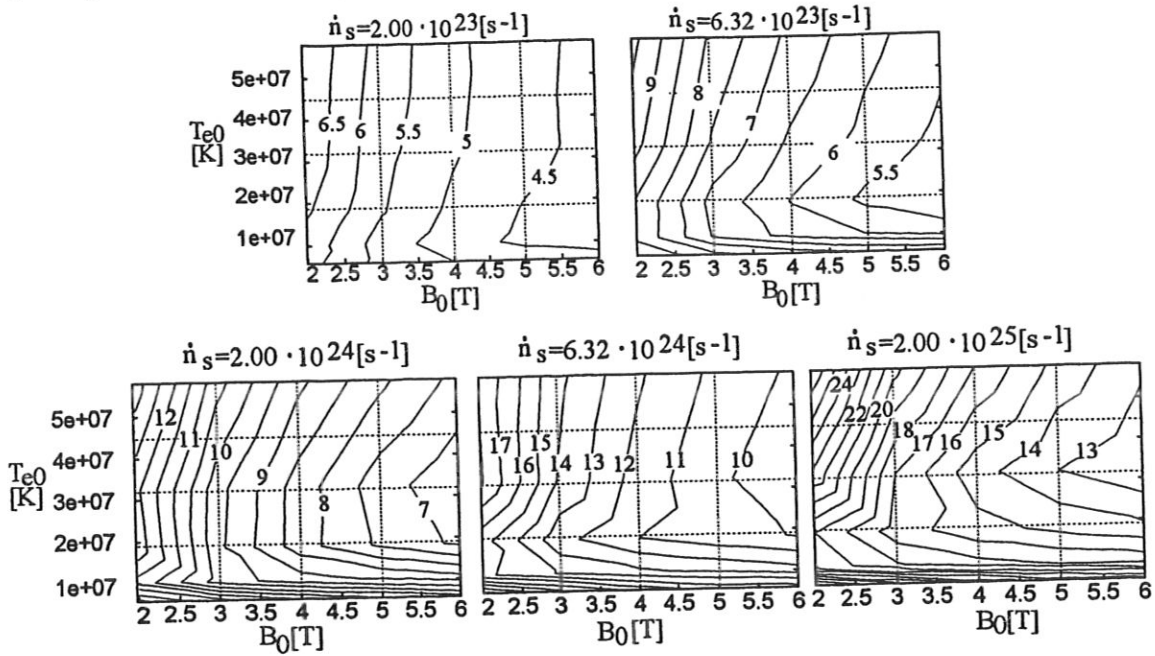

Fig.8.

The contour plots of Fig.8 are based on 125 simulation code runs. In each case, the total time simulated is $t = 20\,\mu s$; the plasma density is $n_{e0} = 5 \cdot 10^{19}\,m^{-3}$; the radius of the pellet is $r_0 = 1\,mm$.

At low plasma temperatures, the radial extension of the cloud is determined primarily by the ionizaton time: an increase of the input plasma temperature causes a decrease of $R_{99\%}$ (low temperature regime: LTR).

At high plasma temperatures, $R_{99\%}$ is controlled by the internal pressure evolving in the cloud. The pressure is able to push the ionized outermost layer of the cloud outward against the $\bar{j} \times \bar{B}$ force. In this case an increase in the plasma temperature is associated with a corresponding increase in $R_{99\%}$, provided that $\dot{n}_s$ and B_0 are constants (high temperature regime: HTR).

Unlike $R_{99\%}$, the ionization radius (the outermost radius where $\alpha = 0.99$) is a monotonous function of T_{e0} and is slightly smaller than or equal to $R_{99\%}$ in LTR, but can be significantly smaller than $R_{99\%}$ in HTR. The cloud radius was found to be proportional to $B_0^{-1/6}$ in LTR and proportional to $B_0^{-1/2}$ in HTR ($\dot{n}_s, T_{e0}$ constant). Another power-law dependence of $R_{99\%}$ on the ablation rate ($\dot{n}_s$) was found to be: $R_{99\%} \propto \dot{n}_s^{1/3}$ in LTR and $R_{99\%} \propto \dot{n}_s^{1/4}$ in HTR.

3.3 Effect of different approximations to the jxB force

In these simulation runs, reactor-grade plasma parameters were used:

$$n_{e0} = 1.5 \cdot 10^{20}\,m^{-3};\quad T_{e0} = 15\,keV;\quad B_0 = 5T;\quad \dot{n}_s = 2 \cdot 10^{26}\,s^{-1};\quad r_{pellet} = 5mm\,.$$

10

The simulation time is $t = 20\,\mu s$ for each case.

The results are displayed in Fig.9. The curves shown correspond to

(a) $\left(\vec{j} \times \vec{B}\right) \cdot \hat{r} = -\sigma\, v_i\, B_0^2$;

(b) $\left(\vec{j} \times \vec{B}\right) \cdot \hat{r} = -\sigma\, v_i\, B^2$; and

(c) $\left(\vec{j} \times \vec{B}\right) \cdot \hat{r} = -\dfrac{\partial p_m}{\partial r}$.

As has been described in section 2.2, the three approximations correspond to the neglect of the magnetic field deformation and the inductive electric field, the neglect of the inductive field only, and to the consistent way of calculating of the $\vec{j} \times \vec{B}$ force, respectively.

As seen in Fig.9, within the framework of the approximation used in the magnetic field calculations (Spitzer conductivity, infinitely long cylinder), a high-beta plasmoid (high-pressure cloud) may cause a reduction of 60 to 80 percent of the magnetic field strength in the cloud interior.

Despite the presence of this partial magnetic cavity, all three models (a)-(c) give similar density distributions. Model (a) shows a significantly higher pressure in the cloud center than shown by the two other models. This is so because model (a) is associated with the strongest undisturbed) magnetic field strength and the strongest deceleration.
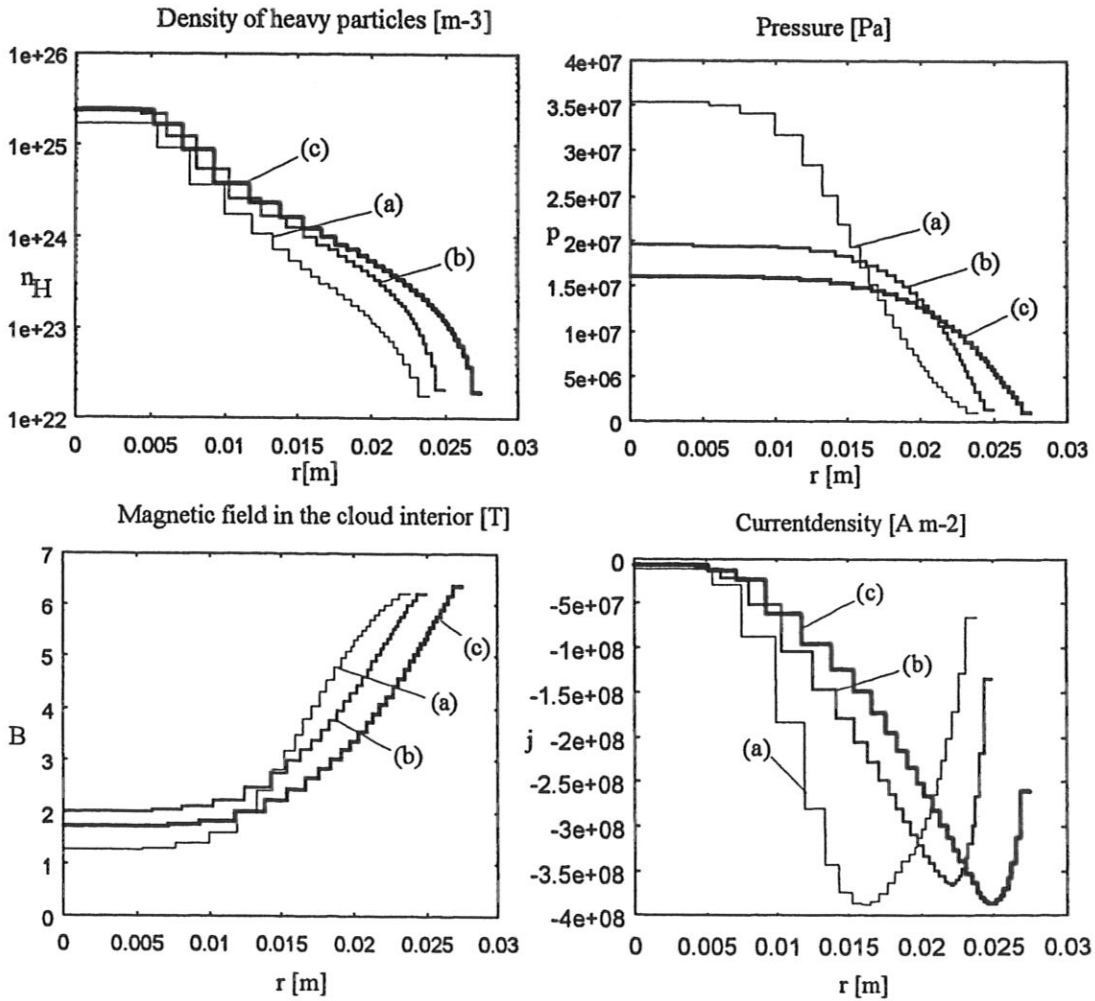

Fig.9.

The three corresponding values of $R_{99\%}$ are:

Modell	$R_{99\%}$ [mm]
(a)	22.3
(b)	23.8
(c)	26.3

3.4 Effect of viscous shear stress

The velocity of axial expansion v_z is a function of time and radial co-ordinate. If $\dfrac{\partial v_z}{\partial r}$ is not zero, then a viscous shear stress (τ_{rz}) acts between the adjacent layers (Lagrangian cells) of the cloud. By modifying the rate of axial expansion, the viscous stress τ_{rz} may affect the velocity profile and the radial distributions of all flow properties.

Only the $\tau_{rz} = \eta \dfrac{\partial v_z}{\partial r}$ component of the viscous stress tensor $\bar{\bar{\tau}}$ is taken into account in the present model. The kinetic viscosity η is assumed to be a weighted average of neutral and ion viscosities:

$$\eta = (1-\alpha)\eta_a + \alpha\,\eta_i$$

where alpha denotes the local ionization degree, and η_a is approximated by the normal state viscosity of H_2 gas:

$$\eta_a \cong 2.4 \cdot 10^5 \,[\mathrm{Pa\,s}]$$

The ion viscosity η_i is calculated on the basis of collisional transport theory:

$$\eta_i = \frac{n_i\,k\,T_i}{\omega_i^2\,\tau_i}[\mathrm{Pa\,s}], \quad \tau_i = 1.14 \cdot 10^7 \frac{T^{1.5}}{\ln\Lambda\,n_i}\,[\mathrm{s}].$$

Due to contact with the surrounding plasma and the resulting local intense heating, the ionized periphery of the cloud shows a faster axial expansion (higher values of v_z) than the neutral internal layers. Viscosity tends to equalise the axial velocities, thus decreasing v_z in the outer layers and increasing it close to axis z.

The results of viscous and inviscid fluid simulations are compared in Fig.10. The simulation parameters are:

$$n_{e0} = 5 \cdot 10^{19}\,\mathrm{m}^{-3},\ T_{e0} = 500\,\mathrm{eV},\ B_0 = 2\,\mathrm{T},\ \dot{n}_{s,tot} = 2 \cdot 10^{23}\,\mathrm{s}^{-1},\ r_{pellet} = 1\,\mathrm{mm}$$

As seen from the graphs, the viscous force does not notably change the cloud radius. The Mach number of the axial flow is decreased below $M_z = 1$ for the major portion of the cloud,

12

and is increased to about $M_z = 2.5$ in the cloud's interior. A corresponding decrease of the heavy particle density occures at the interior of the cloud.
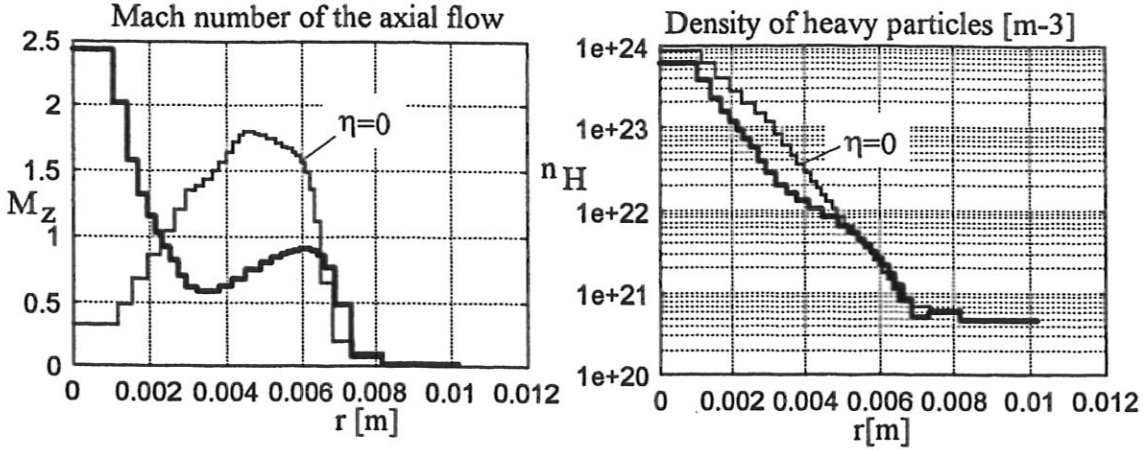

Fig. 10.

3.5 Comparison with previously published simulations

The density distribution of the ablated particles around a stationary pellet in the B-perp direction can properly be approximated by computer models in which the radial expansion dynamics (e.g. the model discussed here) is supplemented by one-dimensional simulation of the axial heating and expansion processes. This axial code can be used, at the same time, for the determination of the ablation rate. This method allows for an economical and simple computing process.

Two such models are available in the literature: one of them developed at IPP-Garching [5] and the other one at CEA Cadarache [7], [8]. In the model developed in Cadarache, the cloud radius is computed on the basis of a single-cell approximation. In the Garching-model, a single-fluid multi-cell Lagrangian code is used for the determination of the cloud radius. Both codes were validated with the help of experimental pellet injection scenarios in Asdex-Upgrade [5] or in Tore Supra [7], [8].

In this section, some of the cloud radii reported for the Asdex-Upgrade [5] and Tore Supra [7] pellet injection shots are recalculated with the present model.

The measured plasma temperature and density distributions used in the simulation runs of [5] can be approximated by the expressions

$$T_{e0} = 1.5[\text{keV}] \cdot \left(1 - \left(\frac{r_{\text{plasma}}}{50[\text{cm}]}\right)^2\right)^2, \quad n_{e0} = 3 \cdot 10^{19}[\text{m}^{-3}] \cdot \left(1 - \left(\frac{r_{\text{plasma}}}{50[\text{cm}]}\right)^2\right).$$

Furthermore, in agreement with experimental data,

$$B_0 = 3\,\text{T}, \ r_{\text{pellet}} = 1\,\text{mm}, \ v_{\text{pellet}} = 1200\frac{\text{m}}{\text{s}}.$$
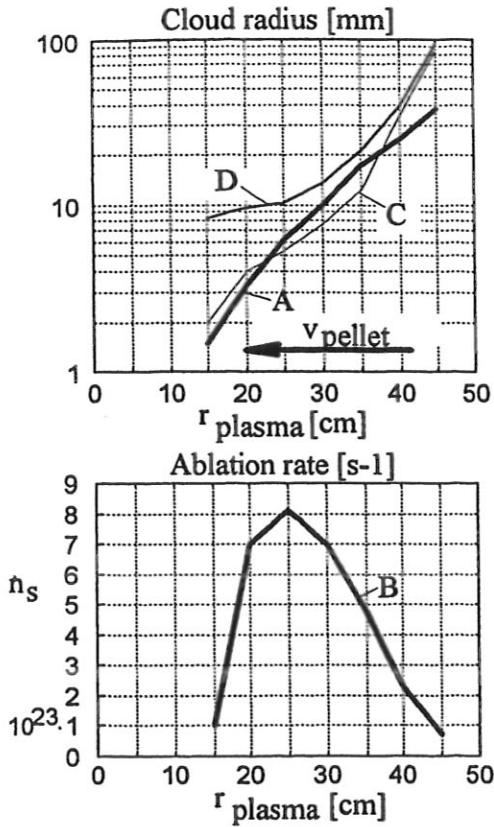
13

Fig.11.

In Fig.11, the variation of the cloud radius along the pellet path obtained with the present model is compared with the corresponding result of [5]. The confinement radius (curve A) and the local ablation rate (curve B) obtained in [5] are reproduced by heavy-set lines in Fig.11.

Two-fluid simulations were carried out for these ablation rates and the coresponding plasma parameters. The ionization radius (curve C) and the radius $R_{99\%}$ (curve D) obtained with the present model are shown by broken lines. As can be seen, the ionization radii computed by the present model (C) are close to the confinement radii (A) obtained by the single fluid model. The $R_{99\%}$ radius obtained with the present model is larger than the the confinement radius of [5] in the entire domain.

Next, the cloud radii reported in [7] for a Tore Supra shot were recomputed with the present model for four positions along the pellet path. The inpute data used in these scenarios and the results obtained are tabulated below. The last column contains the data of [7].

n_{e0} $\left[m^{-3}\right]$	T_{e0} [keV]	B_0 [T]	$\dot{n}_s$ [1/s]	r_{pellet} [mm]	$R_{99\%}$ [mm]	R_{ioniz} [mm]	R_{cld} [mm] Ref:[7]
$1.93 \cdot 10^{19}$	0.58	2.941	$8.12 \cdot 10^{23}$	1.58	11.6	8.0	8.07
$2.65 \cdot 10^{19}$	1.10	3.040	$2.77 \cdot 10^{24}$	1.53	11.7	7.0	10.6
$3.12 \cdot 10^{19}$	1.52	3.143	$4.75 \cdot 10^{24}$	1.42	12.5	6.5	11.8
$3.39 \cdot 10^{19}$	1.80	3.229	$5.70 \cdot 10^{24}$	1.28	12.7	6.0	12.1

As can be seen, the cloud radii computed with the present model are consistently larger than than those reported in [7], similarly to the results of comparison with [5]. At low temperatures, the ionization radii computed with the present model are close to the cloud radii computed for the Tore Supra shot. At high temperatures, better correspondece is observed between our $R_{99\%}$ values and the R_{cld} values computed in Cadarache.

The results of the present calculations were also compared with those stamming from a 2-D Eulerian hydrodynamic code [9]. The simulation parameters used in our run are as follows:

$$n_{e0} = 3 \cdot 10^{19} \, m^{-3}, \ T_{e0} = 1 \, keV, \ B_0 = 3T, \ \dot{n}_s = 2.5 \cdot 10^{24} [1/s], \ r_{pellet} = 2 \, mm, \ t = 4 \, \mu s.$$

The density and ionization degree distributions obtained with the present code are shown in Fig.12. They are in agreement with the results given in Fig.4.11 of [9]. (For being consistent with the single-fluid model of [9], in this simulation the two-fluid feature of our 1-D simulation code was turned-off, that is $v_a = v_i$ was assumed and the momentum equations of the two components were added together.)

14

As seen from the corresponding density plots, the two models give very similar results in terms of cloud radius as well as in terms of range and shape of the density profile. Simulated D_α line emission intensity as given in [9] looks similar to the ionization profile of the present model. The ionization radius is found to be about 9 mm in both calculations.
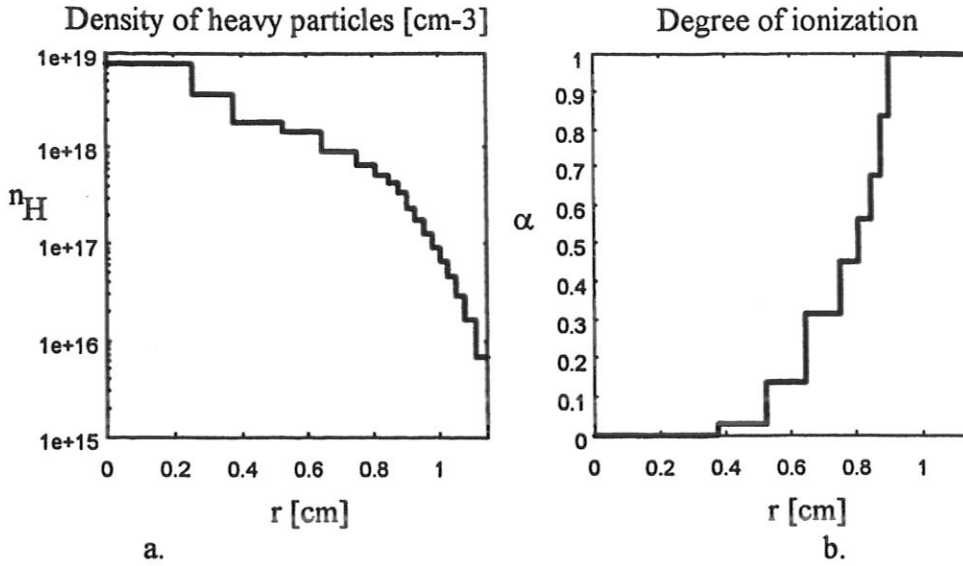

Fig. 12.

3.6 Direct comparison with experimental data

Only a limited number of experimental data are available on the size of the cloud surrounding ablating hydrogen isotope pellets. In an early experiment on ORMAK, the size of the emission region (approximate cloud size) along the pellet path was determined by photographic means [11]. In a simulation run with the present code, the plasma temperature, plasma density, cloud size, and ablation rate measured at the locus of maximum ablation rate in ORMAK were taken as input data (a local pellet radius of 0.1 mm, equal to the initial pellet radius, was assumed in our calculations).

Thus the parameters used in this simulation run were as follows:

$$n_{e0} = 1 \cdot 10^{19} \, \text{m}^{-3}, \quad T_{e0} = 500 \, \text{eV}; \quad B_0 = 1.5 \, \text{T}; \quad \dot{n}_s = 7 \cdot 10^{20} \, \text{s}^{-1}; \quad r_{pellet} = 0.1 \, \text{mm} .$$

It should be noted that this ORMAK shot corresponds to a relatively low plasma density.

This experimental shot, as well as the second one described in this section, were simulated by means of three different approximations described in section 2.2:

    (a) single-fluid approximation,

    (b) stationary ion model,

    (c) the standard two-fluid

model discussed in this report.

The results of comparison with the measurements in ORMAK [11] are displayed in Fig. 13. The radius $R_{observed}$ in Fig. 13 represents the size of the light-emitting region at the point of the highest ablation rate.
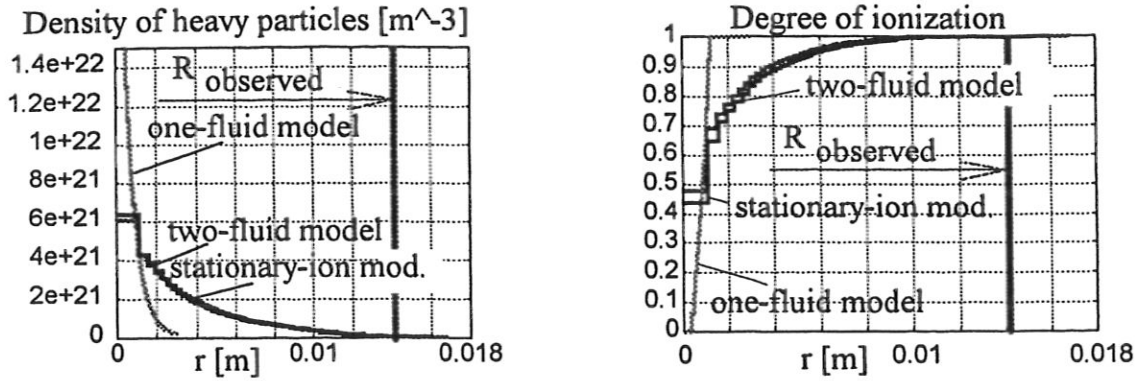
Fig.13.

As shown in Fig.13, the two-fluid simulation gives a cloud radius notably larger than that stemming from the single-fluid model used in the present calculations. Both the two-fluid model and the stationary-ion model agree well with the experimental result considered.

In those cases when a dense ablation cloud is simulated, we find that the two-fluid model and the single-fluid model give nearly the same results, but the stationary-ion simulation usually predicts a somewhat smaller a cloud radius, because v_i is forced to be zero in this model.

In Fig.14 simulated α, n_e, and T profiles are compared with experimental data of DURST et. al. [12]. The ionization radii seen in fast-framing camera images are 5 to 6 millimetres. The electron density and temperature of the visible part of the cloud have been measured spectroscopically.

The simulation parameters are:

$$n_{e0} = 3 \cdot 10^{19} \, m^{-3}, \quad T_{e0} = 500 \, eV; \quad B_0 = 2.8 \, T; \quad \dot{n}_s = 4 \cdot 10^{23} \, s^{-1}; \quad r_{pellet} = 0.5 \, mm.$$
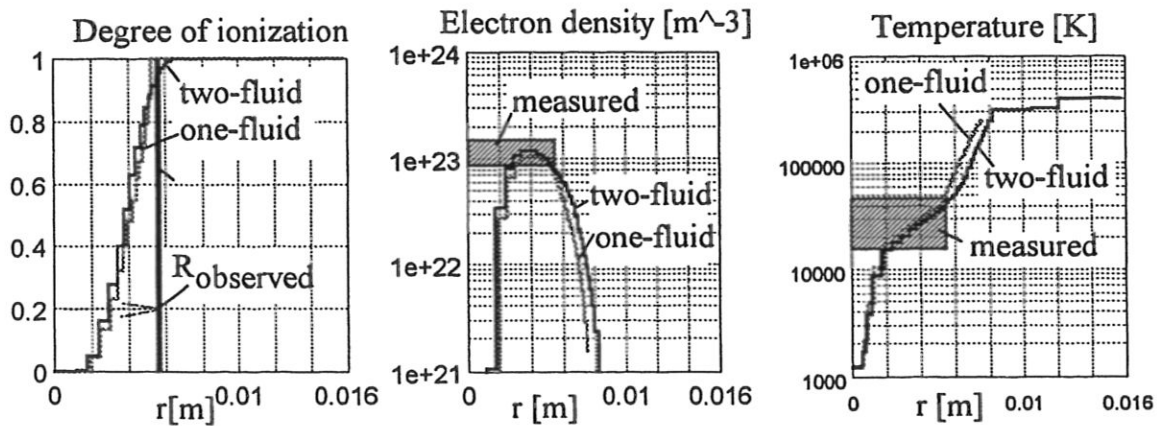

Fig.14.

As can be seen from Fig.14, the two-fluid model and the single-fluid model predict almost the same radial profiles, and both simulations agree well with the experimental observations.

16

4. SUMMARY AND CONCLUSIONS

The results show that the approximately spherically symmetric expansion of the neutral component rapidly changes, due to collisional coupling with the ionized component, into a funnelled flow aligned with the magnetic field lines. This explains the elongated shape of the H_α and H_β emission patterns observed in experiments.

There is a reasonably good agreement between the results obtained with the present two-fluid model and those stemming from simpler approximations: single cell Lagrangian model [7], or multi-cell single-fluid model [5]. Good agreement was found also between the present results and some experimental mesurements.

The two-fluid model calculates consistently somewhat larger stopping radii than the above approximations. On the other hand, the ionization radii computed with the present model are very close to the confinement radii of the other models. The reason for such a behaviour is obvious: the single-fluid models display interaction with the magnetic field (deceleration and stopping of the outer cloud layer, distortion of the magnetic field, etc) as soon as the outer cloud layer starts to become ionized. In a two-fluid model, the neutral component continues to move outward even if the ions are decelerated and stopped by the field, and it may drag the ion component outward because of viscous coupling. Only when a sufficiently large fraction of the cloud becomes ionized, becomes the effect of the magnetic field and of the ion drag (in the reversed direction) overwhelming.

At higher plasma densities, the calculated values of the ionization radius, electron density, cloud temperature, etc., agree well with experimental observations both in the case of two-fluid and single-fluid models.

As time goes on, the outer layers of the cloud are decelerated and depopulated because of rapid axial (field-aligned) expansion of the ablated material. As a result of this, the effective cross-section of the channel available for the axial expansion becomes smaller in time.

This fact should be properly accounted for in computer models aimed at modelling the axial flow dynamics of pellet clouds in magnetically confined plasmas (ablation rate calculations, the origin of striations in pellet clouds, etc.).

Further checks against experimental data, particularly in the low plasma density domain, are needed.

REFERENCES

[1]   S.L.MILORA, C.A.FOSTER, Neutral Gas Shielding Model for Pellet-Plasma Interactions, technical report OAK Ridge National Laboratory ORNL/TM-5776

[2]   W.A. HOULBERG, S.L. MILORA, S.E. ATTENBERGER, Neutral and plasma shielding model for pellet ablation, Nuclear Fusion 28., 595. (1988)

[3]   L.L.LENGYEL, Expansion of dense particle clouds in magnetically confined plasmas, Physics of Fluids 31, 1577. (1988)

[4]   L.L. LENGYEL, G.G. ZAVALA, O.J.W.F. KARDAUN, P. LALOUSIS, Evolution of pellet clouds and cloud structures in magnetically confined plasmas, Nuclear Fusion 31., 1107. (1991)

[5]   L.L. LENGYEL, P.N. SPATHIS, A self-consistent MHD ablation model: pellet penetration depth prediction for a reactor-temperature plasma, Nuclear Fusion 34., 675. (1994)

[6]   G.ZAVALA, Evolution of high-density particle clouds in magnetically confined plasmas, technical report IPP Garghing, IPP 5/33 (1989)

[7]   B. PEGOURIE, J.-M. PICCHIOTTINO, et al., Nucl. Fusion 33 (1993), 591; see also B. PEGOURIE and J.-M. PICCHIOTTINO Plasm Phys. Control. Fusion 35 (1993), B157.

[8]   J.-M. PICCHIOTTINO, Injection de glasons dans un plasma chaud de tokamak: theorie et experience, Ph.D. Thesis, Universite de Provance, Marseille, 1994

[9]   A.K. MACAULAY, et al., Nucl. Fusion 34 (1994), 43.

[10]   D. DÜCHS, Untersuchungen über den Einfluss von Neutralgas auf die Dynamik der Thetapinch-Entladungen, Rept. Nr. IPP 1/14, Max-Planck-Institut für Plasmaphysik, Okt. 1963.

[11]   C.A.FOSTER, R.J.COLCHIN, S.L. MILORA, K. KIM, R.J. TURNBULL, Solid hydrogen pellet injection into the ORMAK Tokamak, Nuclear Fusion 17, 1067, (1977)

[12]   R.D. DURST, W.L. ROWAN, M.E. AUSTIN, R.A. COLLINS, R.F. GANDY, P.E. PHILLIPS, B. RICHARDS, Experimental observation of the dynamics of pellet ablation on the Texas Experimental Tokamak (TEXT), Nuclear Fusion 30. 3. (1990)